3D reconstruction and pore-scale modeling of coated catalytic filters for automotive exhaust gas aftertreatment

Petr Kočí[a,b,*], Martin Isoz[a,c], Marie Plachá[a], Adéla Arvajová[a], Marek Václavík[a], Miloš Svoboda[b], Emily Price[d], Vladimír Novák[d], David Thompsett[d]

[a] University of Chemistry and Technology, Prague, Department of Chemical Engineering, Technická 5, Prague 166 28, Czech Republic
[b] New Technologies Research Centre, University of West Bohemia, Univerzitní 8, Pilsen 306 14, Czech Republic
[c] Czech Academy of Sciences, Institute of Thermomechanics, Dolejškova 5, Prague 182 00, Czech Republic
[d] Johnson Matthey Technology Centre, Blounts Court Road, Sonning Common, Reading RG4 9NH, United Kingdom

A B S T R A C T

This paper introduces a newly developed methodology for the pore-scale simulation of flow, diffusion and reaction in the coated catalytic filter. 3D morphology of the porous filter wall including the actual distribution of catalytic material is reconstructed from X-ray tomography (XRT) images and further validated with the mercury intrusion porosimetry (MIP). The reconstructed medium is then transformed into simulation mesh for OpenFOAM. Flow through free pores in the substrate as well as through the coated zones is simulated by porousSimpleFoam solver, while an in-house developed solver is used for component diffusion and reactions. Three cordierite filter samples with different distribution of alumina-based coating ranging from in-wall to on-wall are examined. Velocity, pressure and component concentration profiles are calculated enabling the prediction of permeability and component conversion depending on the actual microstructure of the wall. The simulation results suggest that the gas predominantly flows through remaining free pores in the filter wall and cracks in the coated layer. The mass transport into the coated domains inside the filter wall is enabled mainly by diffusion. Large domains of compact catalytic coating covering complete channel wall result in a significant increase of pressure drop as the local permeability of the coating is two orders of magnitude smaller than that of bare filter wall.

1. Introduction

Current automotive exhaust gas aftertreatment systems consist of several clean-up devices: catalytic converters for abatement of gaseous pollutants such as CO, hydrocarbons (HC) and nitrogen oxides (NO_x) and a filter trapping the particulate matter (PM). So far only cars with Diesel engines have been equipped with the filter (DPF) but the EURO 6c particulate number limits valid from the year 2017 enforce the use of particulate filters also with gasoline engines (GPF) [1,2]. Both catalyst and filter have the shape of a cylindrical monolith with a large number of parallel channels in a honeycomb arrangement. However, standard catalytic converters are flow-through while the filter channels are alternately plugged at the inlet or outlet so that the exhaust gas is forced to permeate through the porous wall from one channel to another, filtering out the soot [3]. Several different catalysts often need to be combined together to achieve complete conversion of all pollutants [4,5] which makes the exhaust aftertreatment system space-demanding

and delays its heat-up to desired operating temperature.

To make the system more compact, the catalytic materials can be coated in several layers on a single substrate [6,7], or the catalyst can be deposited directly into the filter as on-wall layer or inside the porous wall [3,8]. The frequently used combination for Diesel engines is SCR catalyst for selective catalytic reduction of nitrogen oxides coated on filter (SCRF) [9–11]. Three-way catalyst (TWC) coating is a typical option for gasoline particulate filter [2]. The advantages of catalytic filters are space, weight and cost savings, reduction of overall heat-losses and easier soot combustion in the presence of catalyst [3,8,12–14]. On the other hand, the distribution of catalytic material on or in the porous filter walls has to be carefully optimized to meet the opposing requirements of maximum filtration efficiency, high conversion of gas pollutants, and minimum pressure drop [2,8,11]. Filtration efficiency and pressure loss in the filter depend mainly on size and inter-connectivity of large macropores in the filter wall and spatial distribution of washcoat domains. The gas tends to follow the path of

smallest resistance and flow may by-pass some of the coated zones, leading to undesired slip of unreacted gas components at higher flow rates [9].

In this paper we present recent developments in the methodology for pore-scale simulations of flow, diffusion and catalytic reactions in the wall of catalytic filter. The first attempts of such detailed simulations in diesel particulate filters were reported in the work of Konstandopoulos and co-workers that used lattice Boltzmann method for flow solution combined with finite volume method for component diffusion and reaction in virtually generated material structures [15–18]. Other researchers applied a commercial CFD software to run the flow simulations in 3D reconstructed fibrous filters [19] or ceramic material [20]. The development of X-ray microtomography [21,22] enabled the use of directly reconstructed porous filter in lattice Boltzmann simulation of flow and reactions, although the location of catalytic coating was not explicitly defined [23].

Our current approach enhances the state-of-the-art towards the area of catalytic particulate filters by utilizing the recent developments in 3D imaging of porous structures with multiple solid phases. We apply the XRT for structural characterization of coated filters, revealing actual pore morphology of the substrate as well as spatial distribution of the coating on or inside the filter wall including possible cracks in the coated zones [24,11]. The obtained 3D images are then transformed into simulation domains for solution of convection, diffusion and reaction, providing predictions of flow patterns through the filter wall, catalyst efficiency and wall permeability that affects filter pressure drop. The approach is schematically depicted in Fig. 1. The ultimate goal of detailed models is to obtain quantitative relationship between the material microstructure and its macroscopic properties, similarly as it was accomplished for the catalytic coating of open monoliths [25].

2. 3D reconstruction and characterization of filter morphology

Three samples of particulate filters were examined in this study. All the samples were based on the same commercial cordierite filter substrate and were coated in the lab with γ-Al_2O_3 slurry, dried and calcined. The coating process was controlled to obtain three different distributions: (i) in-wall and (ii, iii) a combination of in-wall and on-wall coating with a different in-wall/on-wall coating volume ratio. These samples were denoted CF1, CF2 and CF3, respectively. For the purpose of this study, γ-Al_2O_3 was not impregnated with platinum group metals as they do not affect porous structure and transport properties of the coating. The γ-Al_2O_3-based coatings are typical for three-way catalysts (TWC), diesel oxidation catalysts (DOC) and NO_x storage catalysts (NSRC, LNT) [7].

A section of an inlet channel was cut out of each filter sample and scanned by X-ray tomograph Xradia MicroXCT 400. The highest achievable resolution with this machine is 0.8 μm with the detector

2048×2048 pixels. During the scanning, the positions of source and detector were fixed while the sample rotated step-wise 360° around its vertical axis. This axis was aligned along the channel. In every position a transmission image of the scanned sample was captured and the final 3D image was reconstructed from the series of 2D projections obtained at different angles of view. The filter samples were scanned with the following parameters: source voltage 60 kV, source power 6 W, voxel size 1.1132 μm, detector resolution 2016×2016 pixels (binning 1), 1800 images per 360° rotation, 7 s exposure of each image, overall scanning time 4.5 h, temperature 28 °C. The samples were imaged with medium-size detector and $10\times$ optical magnification as it offered the best trade-off between the resolution, field of view covering the entire channel cross-section, and contrast necessary to distinguish filter substrate and coated catalyst material.

The used XRT scanner offers two major enhancements to contrast: (i) proprietary phase enhanced detector system, and (ii) propagation-based phase contrast capabilities. The combinations of the detector system with a source operating at low kV and the propagation-based phase contrast technique (by varying source-sample and sample-detector distances) enable the MicroXCT-400 to image both high- and low-Z materials and/or enable to differentiate materials with similar atomic weight. In the case of alumina coated on cordierite substrate, the coating exhibits a lower absorbance and therefore is darker in the resulting image than the substrate. Similar situation occurs with zeolite-based SCR catalyst coated on SiC substrate [11]. In the case of TWC or DOC catalyst formulations containing highly absorbing Ce or Ce–Zr oxides, the coating appears with a higher brightness than the substrate so that it is still possible to perform segmentation of the two solid phases and determine the distribution of active catalytic material in the filter wall.

The XRT resolution was not sufficient to detect small internal pores in the coated zones, therefore additional analyses by mercury intrusion porosimetry (MIP) were necessary to obtain the information about the pore size and porosity of the coating. For each filter sample, small section from the inlet side (1–2 cm^3 in volume) was placed in the measurement cell of a MicroMeritics AutoPore IV 9500 porosimeter. The cells were degassed, filled with mercury and the pressure was increased step-wise (3–60,000 psi) which forced the mercury to intrude pores in the sample. Pore diameter can be directly calculated from applied pressure using Washburn equation [26]. The following values of mercury surface tension and contact angle were used: 485 dyn/cm and 130°, respectively.

The 3D scan (Fig. 2) was exported into a set of 2D slices and further processed using the software package ImageJ-Fiji [27,28]. Examples of single 2D slices (1 of 1600 per 3D scan) are depicted in Fig. 3 – the differences in the washcoat location (on-wall × in-wall) as well as presence of cracks in the on-wall layer can be observed. The full scans were cropped either to $1132 \times 180 \times 1600$ (CF1 sample) or
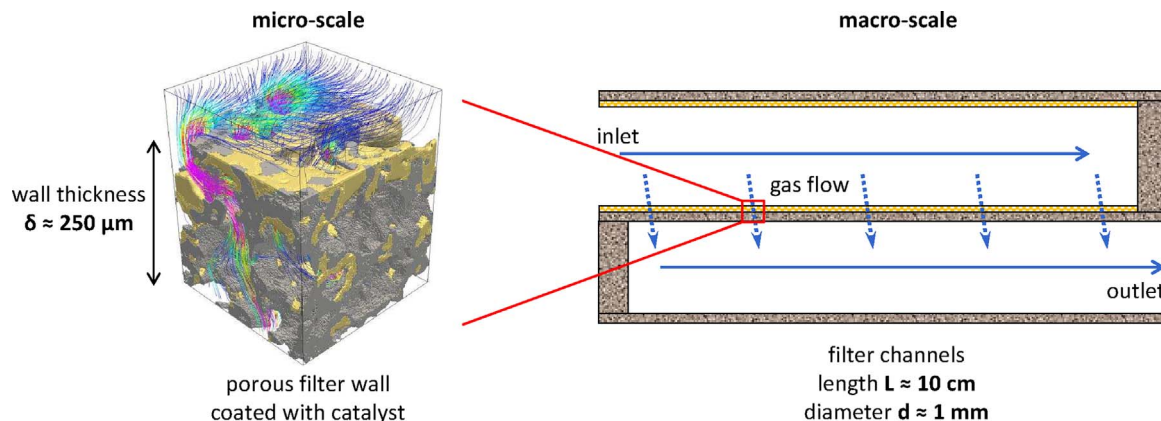

Fig. 1. Schematics of the studied micro-scale system represented by porous filter wall with catalytic coating, and its relation to the full scale of monolithic filter.
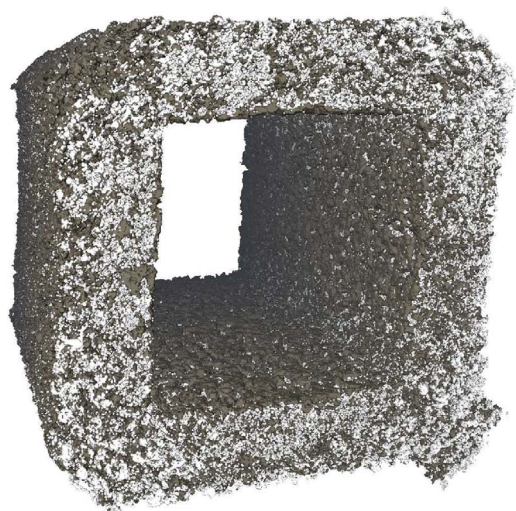
Fig. 2. 3D image of a filter channel reconstructed from the XRT scan.

1132 × 268 × 1600 voxels (CF2, CF3), covering one of the four walls of the filter channel. This crop is marked in green in Fig. 3b and shown in detail in Fig. 4. Brightness and contrast were adjusted and de-noising filters were applied to increase contrast between the individual phases. Finally, the images were thresholded so that each voxel in the image was assigned (according to its brightness) to just one of the three phases: solid filter substrate, alumina coating, or free pore (Fig. 4b).

The segmented media (Fig. 4b) were saved in the form of matrices where the numbers represent the phase present in each voxel. These matrices can be used for evaluation of various morphological descriptors, such as volume fractions of individual phases. In the first example, washcoat loading and distribution in CF1, CF2 and CF3 is compared. It can be seen that while the washcoat volume fractions in all samples are similar, in CF1 the coating is only located inside the wall and in CF2 and CF3 the coating forms a layer on top of the wall. Overall, the on-wall/in-wall coating volume ratio ascends in the order of CF1 < CF2 < CF3 (Fig. 5a).

Fig. 5b compares the average pore volume fraction (= porosity) of the sample CF1 and the uncoated substrate. The addition of coating partially blocks large pores in the substrate, which is reflected both in porosity (CF1 < bare substrate, Fig. 5b) and pore size distribution measured by MIP (Fig. 6a). The pore size distribution shows that CF samples contain pores in three sizes: (i) large macropores in the substrate (approximately 2–50 μm), (ii) smaller macropores in the coating between the alumina particles (100 nm–2 μm), and (iii) mesopores inside the alumina particles ($d < 50$ nm). The smaller macropores inside the coating ($d < 2$ μm) are too close to/under the XRT resolution which results in smaller porosity evaluated by XRT compared to MIP in CF1 sample (Fig. 5b). However, the porosities converge when we do not include the smaller pores ($d < 2$ μm) in the MIP porosity. As expected, both techniques give similar porosities of uncoated substrate (Fig. 5b). A detailed comparison of XRT and MIP characterization techniques applied to the catalytic filters in combination with scanning electron microscopy (SEM) is provided in [11].

In addition to pore size distributions in the coated filters (Fig. 6a), size distribution of alumina particles forming the coating is presented in Fig. 6b. The γ-Al$_2$O$_3$ particle size was measured by static light scattering (Malvern MasterSizer 2000) in the alumina slurry prior to the coating procedure. The particle size distribution corresponds well with the size of smaller macropores detected in the alumina coating (ca. 200 nm–2 μm in Fig. 6a).

The processed and thresholded XRT images were then used for the generation of computational mesh for the subsequent simulations in OpenFOAM [30], an open source C + + library specialized in problems of computational continuum mechanics (CCM) and finite volume
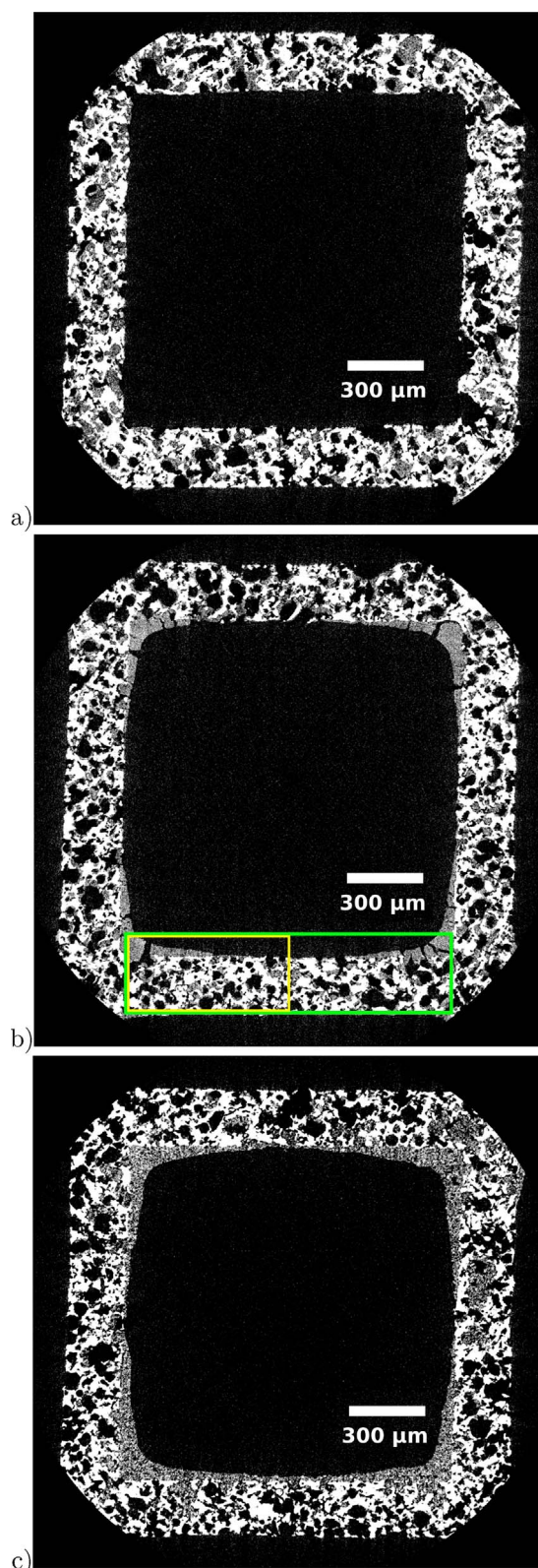

Fig. 3. A single 2D slice from the 3D scan, samples: (a) CF1, (b) CF2, (c) CF3. White: substrate, grey: coating, black: pores. Note the differences in coating distribution.

method. Our selected mesh generator was snappyHexMesh that generates three-dimensional meshes suitable for CCM calculations from triangulated surfaces [30]. Therefore, we first needed to create triangulated surfaces of (i) the filter substrate and (ii) the coated catalytic material, which was done independently in two steps.
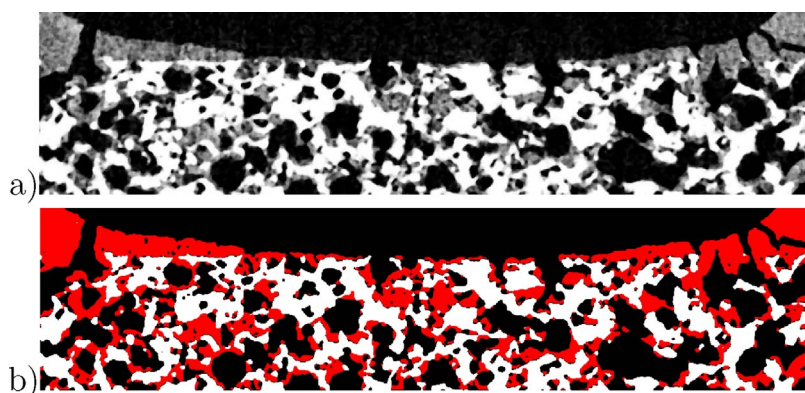
Fig. 4. (a) A detail of the CF2 sample, white: substrate, grey: washcoat, black: pores. (b) The same image after processing and segmentation, the coating is highlighted in red. (For interpretation of the references to colour in this figure legend, the reader is referred to the web version of this article.)
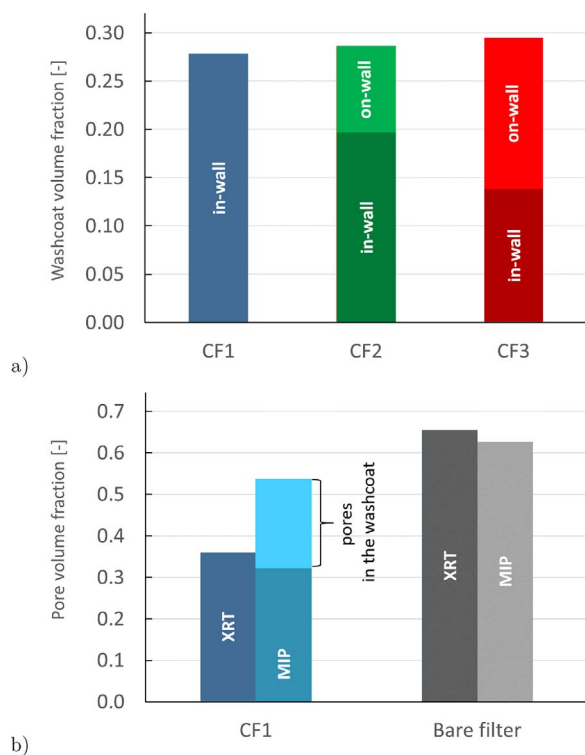

Fig. 5. (a) Volume fraction of coated material and its location evaluated from the XRT scan of the three filter samples. (b) Comparison of pore volume fraction (=porosity) evaluated from the XRT and MIP for bare filter and the coated sample CF1.

Fig. 6. Size distribution of (a) pores in the coated filter (measured by MIP), and (b) γ-Al₂O₃ particles in the coating (measured by light scattering in the slurry prior to coating).

The surface reconstruction algorithm for each phase is based on a consecutive testing of voxels in the thresholded XRT image. If the current voxel corresponds to a solid phase of interest, its neighbours are tested. If the current tested neighbour corresponds to a free pore or if it does not exist (the current voxel is at the system boundary in this direction), the face between the current tested voxel and the current tested neighbour is included in the surface representation.

After the surface reconstruction, snappyHexMesh was applied to create final mesh that involved free pores and coated zones relevant to gas transport and reaction processes. In order to simulate as big part of the filter channel wall as possible while fully resolving all the flow and reaction features we generated unstructured meshes with local refinement in the vicinity of the solid walls and at the coating boundary. A detail of the final mesh structure is depicted in Fig. 7, showing a part of the porous filter wall adjacent to the free channel with dimensions $110 \times 120 \times 110 \, \mu m^3$, consisting of approximately 1.3 million cells. The volume elements in the simulations were performed in a channel section marked by yellow frame in Fig. 3b, covering complete thickness of the filter wall and one half of the channel width. This section has
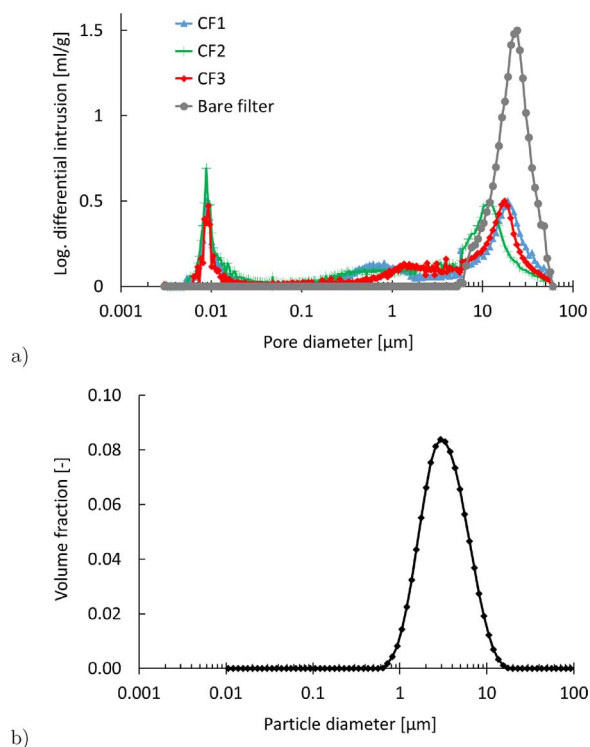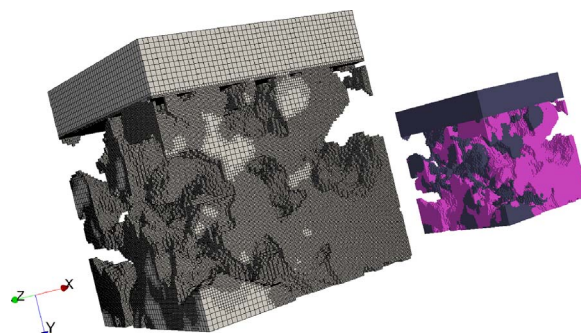

Fig. 7. Example of the used finite volume mesh for a small section of porous filter wall with the coated catalytic material. The mesh covering free pores and coated zones is depicted in the foreground. An auxiliary view with the coating depicted in purple and the free pores in black is shown in the background.

dimensions $630 \times 300 \times 445\,\mu m^3$ and consists of approximately 35 million cells.

3. Mathematical model

The goal of the performed numerical simulations was to obtain approximations of the velocity, pressure and concentration fields in the system corresponding to porous filter wall coated with catalytic material. In all simulations, the studied micro-scale system was considered isothermal and at steady state. Furthermore, we assumed all the constitutive fluids to be incompressible and to form a perfect mixture. The assumption of incompressibility is well acceptable due to relatively small variation of pressure over the studied system.

The applied solution procedure was a segregated one. First, we resolved the flow without taking into account any effects of the reaction. This is justified by low concentrations of reactants, typically present in the exhaust gas from ppm level to few percent, and thus negligible change in total number of moles. Then, the obtained velocity field was used for the subsequent calculations of the concentration fields of the species of interest.

The simulated system is represented in model equations as follows: $\Omega \subset \mathbb{R}^3$ is a simply connected open domain including both the free pores (Ω_p) and the coated zones (Ω_c), such that $\Omega = \Omega_p \cup \Omega_c$ and $\Omega_p \cap \Omega_c = \varnothing$, and Γ is the boundary of the domain Ω.

3.1. Model of flow

A steady state isothermal flow of an incompressible fluid was considered. The characteristic dimension of the flow through open pores in the filter wall was in order of 10^{-5} m and the corresponding Reynolds number in order of 0.1 so that laminar flow was assumed.

To simulate the flow in both open pores (Ω_p) and coated zones (Ω_c) simultaneously, we considered the following variant of the Navier–Stokes equations,

$$\nabla \cdot (\boldsymbol{u} \otimes \boldsymbol{u}) - \nabla \cdot \mathbb{T} = -\nabla p + \boldsymbol{s}$$
$$\nabla \cdot \boldsymbol{u} = 0, \tag{1}$$

where $\boldsymbol{u}$ corresponds to the velocity field, p to the kinematic pressure and $\mathbb{T}$ to the viscous stress tensor defined as $\mathbb{T} = \nu \nabla \boldsymbol{u}$. The coefficient ν denotes the fluid kinematic viscosity. All the external body forces exerted on the fluid are neglected.

The additional source term $\boldsymbol{s}$ in Eq. (1) was obtained from the Darcy permeability model [29] and it is defined as follows,

$$\boldsymbol{s} = \begin{cases} \boldsymbol{0} & \text{in } \Omega_p \\ -\frac{\nu}{\kappa_c}\boldsymbol{u} & \text{in } \Omega_c, \end{cases} \tag{2}$$

where κ_c is the local Darcy permeability through the coated catalytic material.

The system (1) needs to be completed with suitable boundary conditions. The boundary Γ of the solution domain Ω was divided as,

$$\Gamma = \Gamma_{in} \cup \Gamma_{out} \cup \Gamma_{wall}. \tag{3}$$

At the inlet, we prescribed a uniform inlet velocity in the direction of the y axis and a zero-gradient boundary condition for the pressure. A standard no-slip boundary condition was prescribed at the walls. At the outlet, we specified constant pressure and so-called inlet-outlet boundary condition for $\boldsymbol{u}$ that stabilizes the calculation. The complete specification of the applied boundary conditions is given in Table 1.

The numerical solution was performed in the OpenFOAM toolbox [30], employing the porousSimpleFoam steady state solver that uses the consistent SIMPLE algorithm [31,32] to compute the pressure–velocity coupling.

Table 1
Boundary conditions for the flow solution. By y_0 and y_1 we denote the position of the inlet and outlet planes. Symbol $\boldsymbol{n}_\Gamma$ denotes the outer unit normal to the boundary. Symbol $\Phi = \boldsymbol{n}_\Gamma \cdot \boldsymbol{u}$.

Boundary	Condition
$\Gamma_{in} = \{(x, y, z) \in \Gamma : y = y_0,\}$	$\boldsymbol{n}_\Gamma \cdot \nabla p = 0$, $\boldsymbol{u} = (0, u_{in}, 0)^T$
$\Gamma_{out} = \{(x, y, z) \in \Gamma : y = y_1\}$	$p = 0$, $\boldsymbol{n}_\Gamma \cdot \nabla \boldsymbol{u} = (0, 0, 0)^T$ if $\Phi > 0$, otherwise $\boldsymbol{u} = (0, 0, 0)^T$
$\Gamma_{wall} = \Gamma \smallsetminus (\Gamma_{in} \cup \Gamma_{out})$	$\boldsymbol{n}_\Gamma \cdot \nabla p = 0$, $\boldsymbol{u} = (0, 0, 0)^T$

3.2. Model of component diffusion and reaction

The concentration fields of the species of interest were obtained by solving component mole balance in a steady-state diffusion–convection–reaction system. All the species were assumed to be diluted and any effects of the cross-diffusion were neglected. The obtained equation for the i-th specie takes the form of

$$\nabla \cdot (\boldsymbol{u} c_i) - D_i^{eff} \nabla \cdot (\nabla c_i) = r_i, \quad i = 1, ..., n, \tag{4}$$

where c_i denotes the concentration of the i-th specie, D_i^{eff} is the effective diffusion coefficient of the i-th specie and r_i is the source term due to the reaction.

For the case of an isothermal flow in an isobaric environment, it is possible to calculate the total concentration of the gas in the solution domain from the state equation of ideal gas,

$$c_T = \frac{p_T}{R^g T}, \tag{5}$$

where p_T is the mean pressure in the system, R^g is the universal gas constant and T is the system temperature. Utilizing the total concentration, we may change the main variable of interest from the concentrations c_i to the molar fractions of the studied species $y_i = c_i/c_T$. The corresponding modification of (4) for the i-th specie is,

$$\nabla \cdot (\boldsymbol{u} y_i) - D_i^{eff} \nabla \cdot (\nabla y_i) = \frac{r_i}{c_T}, \quad i = 1, ..., n. \tag{6}$$

Because the pressure differences in the system are small compared to the atmospheric pressure, the error introduced by this approximation is, according to our tests, lower than 0.1%.

The free pores in the filter wall (Ω_p) and the coated zones (Ω_c) have significantly different properties from the point of view of both the diffusivity D_i^{eff} and the reaction kinetics r_i. The reaction itself is assumed to take place exclusively in the catalytic coating,

$$r_i = \begin{cases} 0 & \text{in } \Omega_p \\ r_i^c & \text{in } \Omega_c, \end{cases} \tag{7}$$

On the other hand, the internal pore size in the coating is significantly smaller than the size of the free pores in the filter wall. Therefore, the effective diffusivity is calculated as

$$D_i^{eff} = \begin{cases} D_i^{vol} & \text{in } \Omega_p \\ \frac{\varepsilon_{c,M} D_i^{vol}}{\tau_c} & \text{in } \Omega_c, \end{cases} \quad i = 1, ..., n \tag{8}$$

where D_i^{vol} is the volume diffusivity of the i-th specie. The diffusivity through coated zones in porousSimpleFoam is defined by scaling the volume diffusivity by macroporosity $\varepsilon_{c,M}$ and tortuosity τ_c factors of the coated material.

Table 2
Boundary conditions for the solution of the concentration fields.

Boundary	Condition
Γ_{in}	$y_i = y_{i,in}$, $i = 1, ..., n$
$\Gamma_{out} \cup \Gamma_{wall}$	$\boldsymbol{n}_\Gamma \cdot \nabla y_i = 0$, $i = 1, ..., n$

To complete Eq. (6) we applied a Dirichlet boundary condition at inlet to fix the concentrations of reactants there. At Γ_{out} and Γ_{wall} the zero-gradient boundary condition was applied. The complete specification of the respective subsets of Γ and of the applied boundary conditions is given in Table 2.

The system (6) is solved via the means of the OpenFOAM library with a user-defined solver. The solution is based on the finite volume method [33] and it has a few specifics.

First, the Dirichlet boundary condition imposed at the inlet behaves effectively as the Danckwerts boundary condition [34]. To describe the situation, let us for a moment assume a one-dimensional problem. At the inlet and for the i-th specie, we impose the condition $\boldsymbol{u} = \boldsymbol{u}_{in}$, $y_i = y_{i,in}$. In other words, we prescribe the inflow of the i-th specie into the solution domain,

$$f_{i,in} = \int_{\Gamma_{in}} \boldsymbol{n}_\Gamma \cdot \boldsymbol{u}_{in} y_{i,in}\, dS, \quad i = 1, ..., n. \tag{9}$$

Now, let us denote the discretization of the solution domain Ω into the finite volume cells as Ω^h. Furthermore, let Ω_P^h be the cell adjacent to the boundary and Ω_N^h its neighbour inside the domain. The balance for the i-th specie in the cell Ω_P^h is

$$f_{i,in} = f_{i,P \to N} + \int_{\Omega_P^h} r_i\, dV = \int_{\Gamma_{PN}} \boldsymbol{n}_{\Gamma_{PN}} \cdot (\boldsymbol{u} y_{i,P} - D_i^{eff} \nabla y_{i,P})\, dS + \int_{\Omega_P^h} r_i\, dV, \tag{10}$$

where by $f_{i,P \to N}$ we denote the flux of the i-th specie from the cell Ω_P^h to the cell Ω_N^h and by Γ_{PN} the face between the cells Ω_P^h and Ω_N^h. Enforcing the balance equation (10) including the diffusion flux then causes a Danckwerts-like jump in the concentration field between the inlet boundary and the cells adjacent to it.

The second particularity connected to the usage of the OpenFOAM library is the fact that the system (6) is solved in a segregated manner, i.e., for each component separately, iteratively and in a linearized form. The only possibly non-linear term in (6) is the reaction rate r_i. The term r_i, $i = 1, ..., n$, linearized at k-th iteration takes the form of,

$$r_i \approx r_i(\boldsymbol{y}^{(aux)}) + \frac{\partial r_i}{\partial y_i}(\boldsymbol{y}^{(aux)})(y_i^{(k)} - y_i^{(k-1)})$$
$$\boldsymbol{y}^{(aux)} = (y_1^{(k)}, ..., y_{i-1}^{(k)}, y_i^{(k-1)}, ..., y_n^{(k-1)})^T, \tag{11}$$

which coincides with the Taylor expansion of the term r_i with respect to y_i around the point y_i^{k-1}. Also, mind that when dealing with the i-th component of $\boldsymbol{y}$, the components $y_1, ..., y_{i-1}$ have already been updated. The updated values are used in the approximation of the term r_i.

For the purpose of this study, CO oxidation was considered as a model reaction in the catalytic filter:

$$CO + \frac{1}{2}O_2 \to CO_2. \tag{12}$$

The steady-state reaction kinetics of CO oxidation on Pt/γ-Al$_2$O$_3$ catalyst [35] was employed:

$$r = k\frac{y_{CO}y_{O_2}}{(1 + K_{inh}y_{CO})^2}, \tag{13}$$

where k and K_{inh} are the reaction and inhibition constants, respectively, obtained from the corresponding Arrhenius relations,

$$k = k_0 \exp\left(\frac{-E_a}{R^g T}\right), \quad K_{inh} = K_0 \exp\left(\frac{E}{T}\right). \tag{14}$$

The component reaction rates of CO, O$_2$ and CO$_2$ were obtained as

$$r_i = \tilde{\nu}_i r, \quad i = CO, O_2, CO_2, \tag{15}$$

with $\tilde{\nu}_i$ being the respective stoichiometric coefficients.

3.3. Model parameter values

The parameters characterizing internal structure of the coating are presented in Table 3. The coating macroporosity $\varepsilon_{c,M}$ was evaluated

Table 3
Structural parameters of the coated material.

Parameter	Symbol	Value
Macroporosity	$\varepsilon_{c,M}$	0.30
Mean macropore diameter	$\bar{d}_M$	1 μm
Mesoporosity	$\varepsilon_{c,m}$	0.38
Mean mesopore diameter	$\bar{d}_m$	10 nm
Mean particle diameter	d_P	3 μm

from the MIP intrusion curve as the volume fraction of relevant pores in the range 50 nm–3 μm (Fig. 6a), related to the volume of the coating. The mean macropore size $\bar{d}_M$ was calculated from the MIP pore size distribution in the same range of pore sizes. Similar procedure was repeated for mesoporosity $\varepsilon_{c,m}$ and mean mesopore size $\bar{d}_m$, taking into account pore size range 2–50 nm. Note that the mesoporosity $\varepsilon_{c,m}$ defined here is also related to the total volume of the coating. The mean γ-Al$_2$O$_3$ particle diameter was calculated from the γ-Al$_2$O$_3$ particle size distribution (Fig. 6b). Variation of these parameters among the samples CF1, CF2 and CF3 was only minor so that the same (averaged) values given in Table 3 were used for modeling of the coated zones in all samples.

The value of mean macropore diameter $\bar{d}_M$ indicates that only volume diffusion is relevant to macropores [25]. The correlation (16) for volume diffusivity of the ith specie in the reference gas "ref" was adopted from [36]:

$$D_i^{vol} = \frac{1.449 \ast 10^{-2}\, T^{1.75}/p}{\sqrt{2/(10^{-3}/M_i + 10^{-3}/M_{ref})}(\sigma_i^{1/3} + \sigma_{ref}^{1/3})^2}, \tag{16}$$

where σ_i is the diffusion volume of the component i (20.1, 18.9, 16.6 and 26.9 m^3/mol for air, CO, O$_2$ and CO$_2$, respectively) [36]. Air was considered as the reference component (carrier gas).

In small mesopores, the transport is dominated by Knudsen diffusion and the local diffusivity is calculated as follows:

$$D_i^{Kn} = \frac{\bar{d}_m}{3}\sqrt{\frac{8R^g T}{M_i \pi}} \tag{17}$$

The overall effective diffusivity through the coated material is then calculated from the random-pore model considering the contributions of both larger macropores and smaller mesopores [37]:

$$D_i^{eff} = \varepsilon_{c,M}{}^2 D_i^{vol} + \varepsilon_{c,m}{}^2 D_i^{Kn} + \frac{4(\varepsilon_{c,M} - \varepsilon_{c,M}^2)}{((1/D_i^{vol}) + ((1 - \varepsilon_{c,M})^2/\varepsilon_{c,m}^2 D_i^{Kn}))}. \tag{18}$$

Having the estimate of effective diffusion coefficient D_i^{eff} in the coating from the random pore model (18), the tortuosity factor τ_c required by porousSimpleFoam is calculated from Eq. (8) using the known coating macroporosity $\varepsilon_{c,M}$. The resulting tortuosity value for the coated zones with the parameters given in Table 3 is $\tau_c = 3.3$.

The Darcy permeability of the coated material κ_c is estimated from the Carman–Kozeny equation [38]:

$$\kappa_c = \frac{d_P^2 \varepsilon_{c,M}^3}{36k_K(1 - \varepsilon_{c,M})^2}, \tag{19}$$

where d_P is the mean particle diameter in porous coated zone (see Table 3). The Kozeny constant k_K is approximated by the value 5.0, see the discussion in [39]. The resulting estimate of permeability κ_c in the coated zones is then 2.76×10^{-15} m^2 which equals to 0.00276 Da.

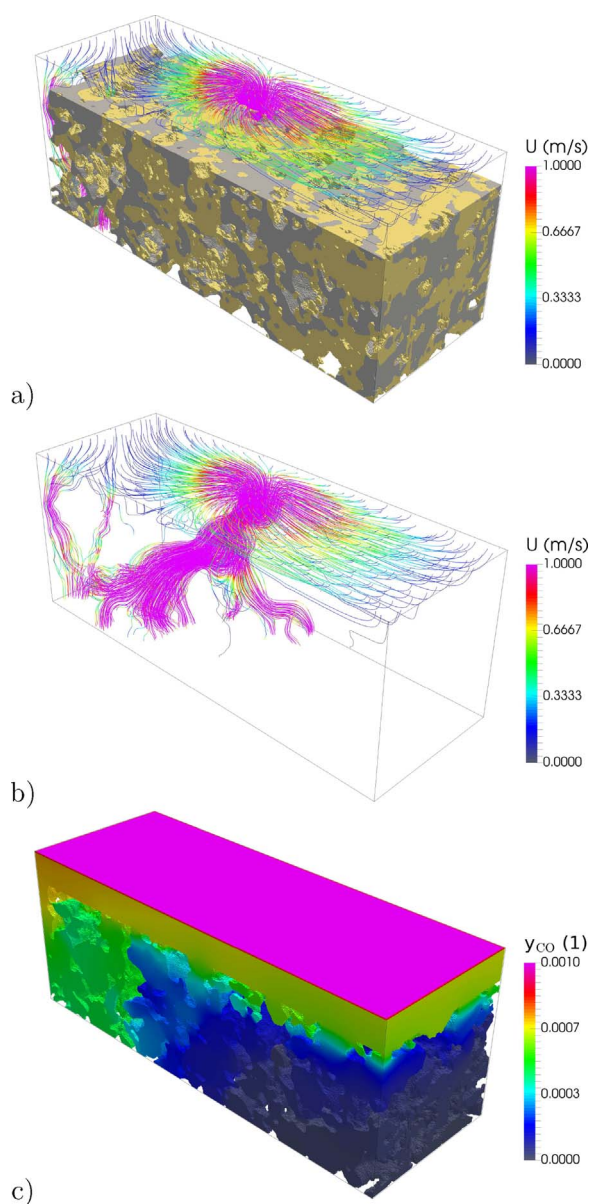Kinematic viscosity ν of the gas flowing through the filter wall was calculated from:

$$\nu = \frac{\mu}{\rho}, \tag{20}$$

$$\mu = \frac{bT^{3/2}}{T + S}, \tag{21}$$

Table 4
The values of reaction kinetics parameters.

Parameter	Value	Unit
k_0	7.84×10^{16}	$\mathrm{mol\,s^{-1}\,m^{-3}}$
E_a	90×10^3	$\mathrm{J\,mol^{-1}}$
K_0	80	1
E	1×10^3	K

a)

b)

c)

Fig. 8. Section of filter sample CF1 (in-wall coating) at $T = 453\,\mathrm{K}$: (a) reconstructed wall structure (substrate = grey, catalytic coating = yellow) with streamlines of gas flow, (b) streamlines in the complete volume of the simulated domain, and (c) CO concentration profile. (For interpretation of the references to colour in this figure legend, the reader is referred to the web version of this article.)

where ρ is density computed from the ideal gas equation and μ stands for the dynamic viscosity given by Sutherland equation (21), with the parameters $b = 1.458 \times 10^{-6}\,\mathrm{kg\,m^2\,s^{-1}\,K^{-1/2}}$ and $S = 110.4\,\mathrm{K}$.

The reaction kinetic parameters for CO oxidation on Pt/γ-Al$_2$O$_3$ were adapted from [25] and their values are summarized in Table 4. In this paper, we use the original rate law according to [35] without any extension so that the rate constant k_0 in Table 4 corresponds to
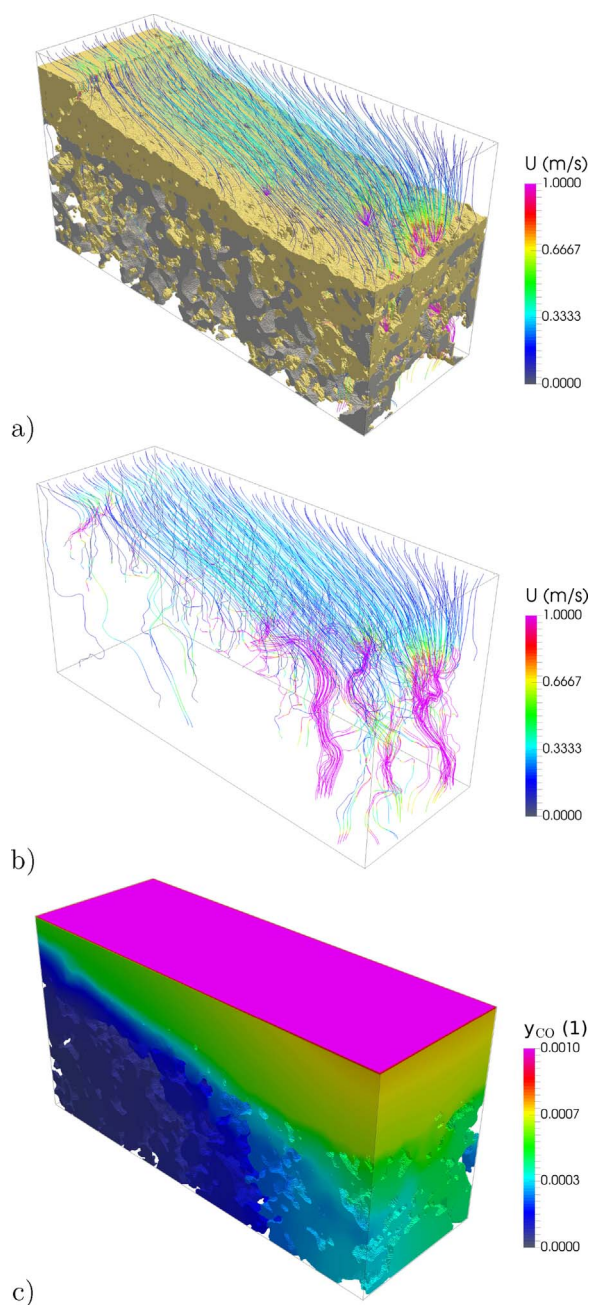

a)

b)

c)
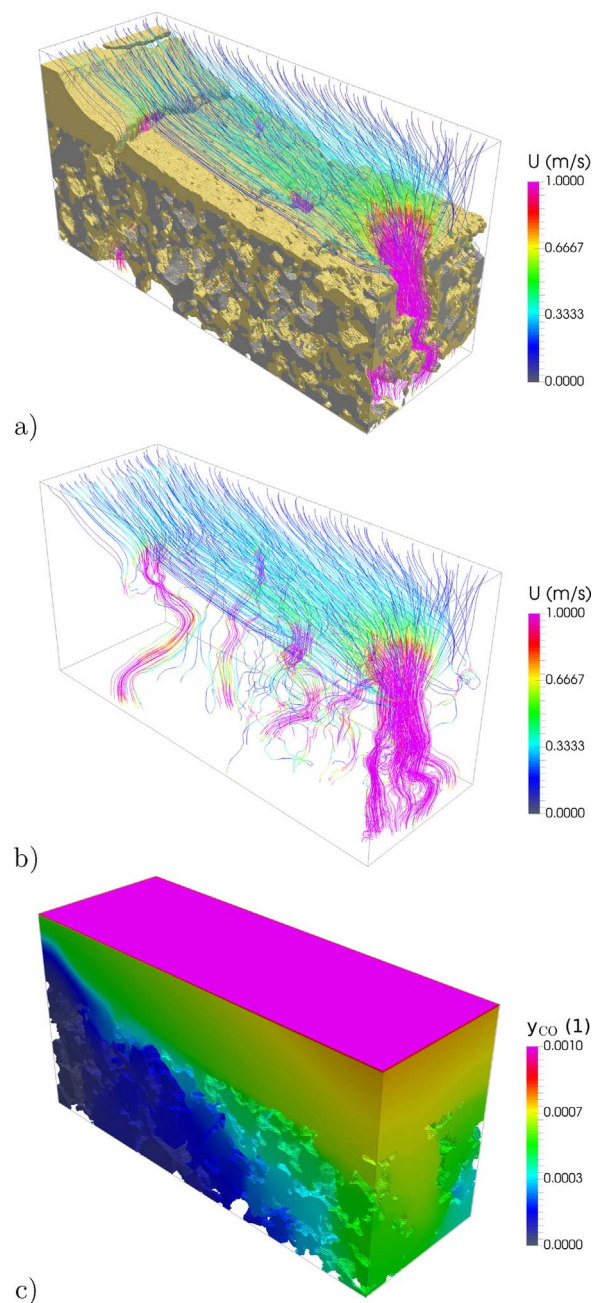
Fig. 9. Section of filter sample CF2 (combined in-wall and on-wall coating) at $T = 453\,\mathrm{K}$: (a) reconstructed wall structure (substrate = grey, catalytic coating = yellow) with streamlines of gas flow, (b) streamlines in the complete volume of the simulated domain, and (c) CO concentration profile. (For interpretation of the references to colour in this figure legend, the reader is referred to the web version of this article.)

$C_{\mathrm{Pt}}^{\mu} k_{0,\mathrm{CO}}/T$ reported in [25].

4. Results

Examples of gas velocity and CO concentration profiles obtained by convection–diffusion–reaction simulation in the section of catalytic filter wall are shown in Figs. 8–10. The simulation temperature 453 K was selected close to the light-off for CO oxidation in order to clearly reveal the differences in CO conversion between the individual samples. For each filter sample (CF1, CF2 and CF3), the simulation was repeated with eight different sections to obtain statistically representative results. The overall permeability of the coated filter wall κ^{avg} was then evaluated from the Darcy equation utilizing the calculated average

a)

b)

c)

Fig. 10. Section of filter sample CF3 (compact on-wall coating combined with in-wall) at $T = 453$ K: (a) reconstructed wall structure (substrate = grey, catalytic coating = yellow) with streamlines of gas flow, (b) streamlines in the complete volume of the simulated domain, and (c) CO concentration profile. (For interpretation of the references to colour in this figure legend, the reader is referred to the web version of this article.)

pressure drop over the simulated system Δp^{avg}:

$$\kappa^{\mathrm{avg}} = \frac{u_{\mathrm{in}}\mu\delta^{\mathrm{avg}}}{\Delta p^{\mathrm{avg}}}, \tag{22}$$

where δ^{avg} denotes mean thickness of the coated wall in direction of the imposed flow (y axis in our case). Note that in the laminar regime with low Reynolds number the evaluated permeability of the wall does not depend on the chosen gas velocity, viscosity and wall thickness, which makes this parameter suitable for the comparison between different filter structures. The filter wall with a higher permeability exhibits a lower pressure drop at the same flow rate, which is desired for the application in the automotive exhaust gas aftertreatment.

The calculated overall permeabilities of the studied samples CF1,
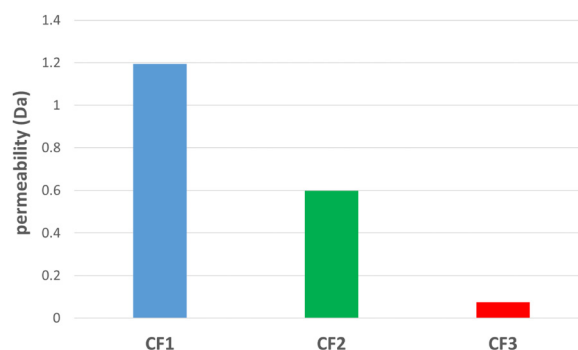
Fig. 11. Predicted overall permeability of the filter wall with different distribution of catalytic coating (averaged over 8 different sections of each sample).

CF2 and CF3 are summarized in Fig. 11. For each sample, the results were obtained by averaging the permeabilities κ^{avg} obtained in flow simulations of eight different sections. To understand the background of these results, it is necessary to analyse the calculated velocity and concentration profiles for the individual distributions of the coated material in more detail.

The catalytic coating in the sample CF1 is located completely inside wall pores (Fig. 8). The flow pattern in the given section is quite non-uniform. Majority of the substrate pores is completely blocked by the catalytic material but there still exist few unrestricted pathways through incompletely coated substrate pores. These open pathways are predominantly used for the gas flow (Fig. 8a and b) because the local permeability of the coated zones is more than two orders of magnitude lower (0.00276 Da as predicted from Eq. (19)). This results in a slip of unreacted CO as the local velocity on the dominant pathway is quite high (an order-of-magnitude higher than averaged superficial velocity through the filter wall), and gas transport into the coated zones is limited mostly to relatively slow diffusion (Fig. 8c). On the other hand, the permeability of this sample is the highest of the studied ones (Fig. 11), which corresponds to the lowest pressure drop over the wall.

The sample CF2 exhibits more uniform flow distribution over the studied domain (Fig. 9). The streamlines reveal that the flow pattern is largely influenced by the cracks in the layer coated on top of the wall (Fig. 9a and b). Slightly higher loading of catalytic material in combination with more uniform flow distribution results in a lower CO slip and higher conversion than in the case of CF1 sample (Fig. 8c). The relatively large number of small cracks provides open pathways for the gas flow and helps to keep the overall wall permeability of the CF2 sample reasonably high (Fig. 11).

The layer coated on top of the wall in the sample CF3 (Fig. 10) is almost crack-free. In this case, the gas is forced to flow uniformly through the coated layer (Fig. 10a and b). The improved mass transfer results in the lowest slip of unreacted CO (Fig. 10c). However, this result is counter-balanced by the significantly lower overall permeability of the CF3 filter wall (Fig. 11) resulting in a quite high pressure drop. This is in line with the previous findings that the filter coated with a compact on-wall layer results in a higher initial pressure drop of a clean filter. Even if this configuration may offer a better filtration efficiency and a milder and more linear increase of pressure drop during soot accumulation [40], the nominal pressure drop of a clean CF3 filter would probably disqualify it from the practical application in automotive exhaust gas aftertreatment.

The CO conversion profiles in the sections of samples CF1, CF2 and CF3 are compared in Fig. 12. The profiles are averaged in xz plane and plotted along the imposed flow direction (y axis, inlet at y_0, outlet at y_1, see Table 1). The conversion profiles reflect spatial distribution of the catalytic coating in each sample. The onset of CO conversion in the sample CF1 corresponds to the substrate wall boundary as the catalytic material in this sample is located only inside the wall pores. The samples CF2 and CF3 possess also catalytic layer on top of the wall which
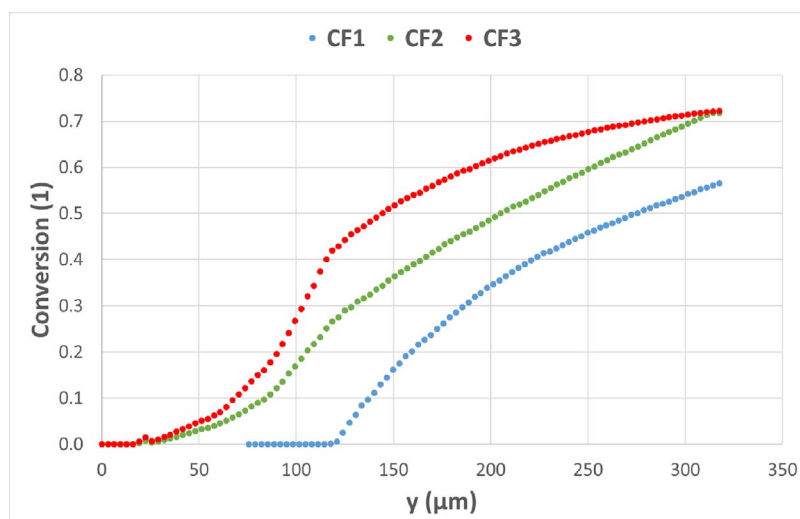
Fig. 12. CO conversion profile across the filter wall with different distribution of catalytic coating (averaged over 8 different sections of each sample).

shifts the CO conversion onset upstream. The sample CF3 shows the steepest initial increase of conversion but there is almost no further increase deeper in the wall due to the lack of catalytic material (majority of the coating is located on and in the upper part of the wall). This represents a potential risk in the case of cracks or other defects in the coated layer. The samples CF1 and CF2 exhibit much more uniform increase of conversion inside the wall.

The outlet CO conversion in Fig. 12 is similar for the samples CF2 and CF3, while the extent of CO oxidation in CF1 is somewhat lower. When we combine these findings with the calculated permeabilities in Fig. 11 , we can characterize the performance of the studied samples in the following way: CF1 provides the lowest pressure drop but also the lowest conversion. The sample CF3 achieves a higher conversion, however, at the expense of a high pressure drop (i.e., very low permeability). The sample CF2 reaches the same conversion as CF3 while keeping a relatively high permeability, which represents a reasonable compromise between the conversion and pressure drop demands.

The necessary condition for obtaining meaningful output from the detailed pore-scale simulations is to have a sufficiently large domain that contains statistical representation of the morphological features present in the studied system. In our case we chose the simulated section size in such a way that its height covers complete wall thickness, width one half of the channel, and the depth similar to wall thickness. The reason is that this system can be comfortably simulated on a current standard desktop computer with 128 GB RAM, avoiding the need for special computers and making the methodology accessible for common users. However, the flow profiles given in Figs. 8–10 reveal that there might be just few open pathways for flow in such domain. Therefore the simulations were repeated with eight different sections from each sample in order to obtain average results that are statistically representative. The variation of permeability in the individual sections is illustrated in Fig. 13. The lowest variation is observed for the CF2 and CF3 samples with on-wall coating (except one CF3 section with a significantly higher permeability resulting from the local non-uniformity of the coating). The variation in all samples is obviously related to the existence of major open pathways through the wall—they significantly increase the permeability. This situation occurs most frequently in the sample CF1 with the coating located only inside the wall.

5. Conclusions

The detailed pore-scale models of reaction and transport in combination with X-ray tomography represent powerful tools that are able to predict macroscopic properties such as permeability (pressure drop) and conversion in the filter wall depending on its microstructure. The

a)

b)

c)
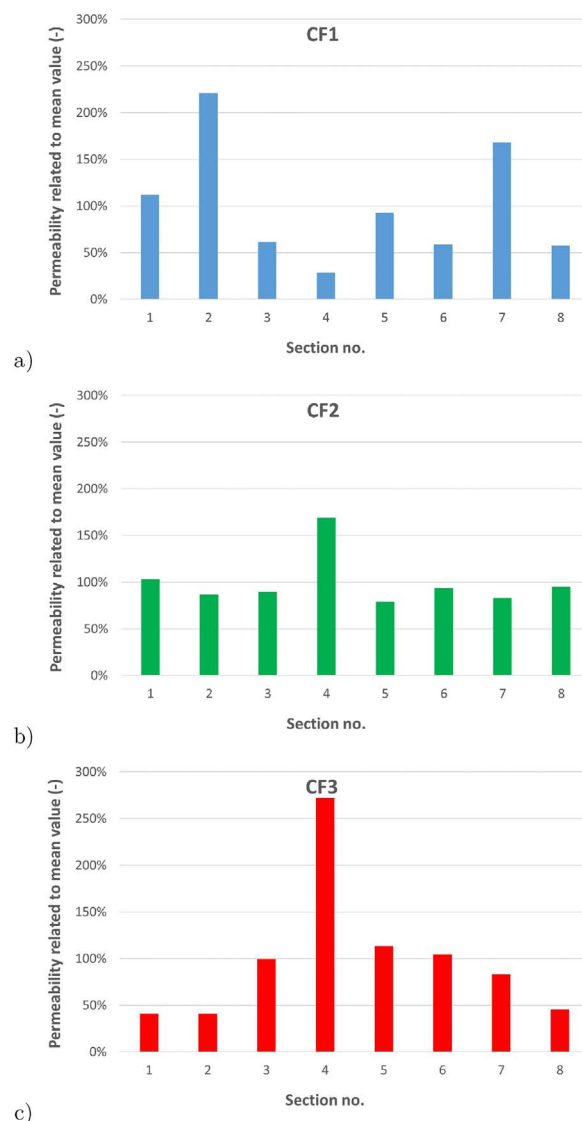
Fig. 13. Relative variation of the wall permeability in individual sections of the filter samples.

results presented for three different distributions of catalytic coating cover the range of structures varying from completely in-wall coating to the coating with majority of the material in a layer on top of the wall.

The results suggest that the gas predominantly flows through cracks in the coated layer and remaining free pores in the filter wall. The mass transport into the coated zones inside the filter wall is enabled mainly by diffusion. Large domains of compact catalytic coating covering complete channel wall result in a significant increase of pressure drop as the local permeability of the coating is more than two orders of magnitude smaller than that of bare filter wall. On the other hand, the samples with on-wall coating exhibit increased conversion of pollutants. From the studied samples, the most promising structure was CF2 combining in-wall and partial on-wall coating.

The developed models open the doors to computer-aided optimization of coating distribution in particulate filters, aiming on a balanced performance with respect to the pressure drop, filtration efficiency and conversion of gas components.

Acknowledgments

References

[1] T. Johnson, Vehicular emissions in review, SAE Int. J. Engines 9 (2016) 1258–1275.

[2] C. Lambert, T. Chanko, D. Dobson, X. Liu, J. Pakko, Gasoline particle filter development, Emission Control Sci. Technol. 3 (2017) 105–111.

[3] B. Guan, R. Zhan, H. Lin, Z. Huang, Review of the state-of-the-art of exhaust particulate filter technology in internal combustion engines, J. Environ. Manag. 154 (2015) 225–258.

[4] A. Güthenke, D. Chatterjee, M. Weibel, B. Krutzsch, P. Kočí, M. Marek, I. Nova, E. Tronconi, Current status of modeling lean exhaust gas aftertreatment catalysts, Adv. Chem. Eng. 33 (2007) 103–211.

[5] D. Chatterjee, P. Kočí, V. Schmeißer, M. Marek, M. Weibel, B. Krutzsch, Modelling of a combined NO_x storage and NH_3-SCR catalytic system for diesel exhaust gas aftertreatment, Catal. Today 151 (2010) 395–409.

[6] Y. Zheng, Y. Liu, M.P. Harold, D. Luss, LNT-SCR dual-layer catalysts optimized for lean NO_x reduction by H_2 and CO, Appl. Catal. B: Environ. 148–149 (2014) 311–321.

[7] M. Václavík, V. Novák, J. Březina, P. Kočí, G. Gregori, D. Thompsett, Effect of diffusion limitation on the performance of multi-layer oxidation and lean NO_x trap catalysts, Catal. Today 273 (2016) 112–120.

[8] G. Koltsakis, O. Haralampous, C. Depcik, J.C. Ragone, Catalyzed diesel particulate filter modeling, Rev. Chem. Eng. 29 (2013) 1–61.

[9] G. Cavataio, J.W. Girard, C.K. Lambert, Cu/Zeolite SCR on High Porosity Filters: Laboratory and Engine Performance Evaluations, SAE Technical Paper 2009-01-0897, (2009).

[10] T.C. Watling, M.R. Ravenscroft, G. Avery, Development, validation and application of a model for an SCR catalyst coated diesel particulate filter, Catal. Today 188 (2012) 32–41.

[11] M. Václavík, M. Plachá, P. Kočí, M. Svoboda, T. Hotchkiss, V. Novák, D. Thompsett, Structure characterisation of catalytic particulate filters for automotive exhaust gas aftertreatment, Mater. Charact. 134 (2017) 311–318.

[12] O.A. Haralampous, G.C. Koltsakis, Z.C. Samaras, C.D. Vogt, E. Ohara, Y. Watanabe, T. Mizutani, Reaction and Diffusion Phenomena in Catalyzed Diesel Particulate Filters, SAE Technical Paper 2004-01-0696, (2014).

[13] M. Schejbal, M. Marek, M. Kubíček, P. Kočí, Modelling of diesel filters for particulates removal, Chem. Eng. J. 154 (2009) 219–230.

[14] M. Schejbal, J. Štěpánek, M. Marek, P. Kočí, M. Kubíček, Modelling of soot oxidation by NO_2 in various types of diesel particulate filters, Fuel 89 (2010) 2365–2375.

[15] N.D. Vlachos, A.G. Konstandopoulos, Digital Materials Methods for DPF Development, SAE Technical Paper 2006-01-0260, (2006).

[16] A.G. Konstandopoulos, N.D. Vlachos, G. Patrianakos, Application of Digital Material Methods to Silicon Carbide Diesel Particulate Filters, SAE Technical Paper 2007-01-1131, (2007).

[17] N.D. Vlachos, G. Patrianakos, M. Kostoglou, A.G. Konstandopoulos, Micro-Simulation of NO-NO_2 Transport and Reaction in the Wall of a Catalyzed Diesel Particulate Filter, SAE Technical Paper 2008-01-0442, (2008).

[18] A.G. Konstandopoulos, M. Kostoglou, S. Lorentzou, N. Vlachos, Aspects of multifunctional diesel particulate filters and their efficient simulation, Catal. Today 188 (2012) 2–13.

[19] S. Jaganathan, H. Vahedi Tafreshi, B. Pourdeyhimi, A realistic approach for modeling permeability of fibrous media: 3-D imaging coupled with CFD simulation, Chem. Eng. Sci. 63 (2008) 244–252.

[20] J. Petrasch, F. Meier, H. Friess, A. Steinfeld, Tomography based determination of permeability, Dupuit–Forchheimer coefficient, and interfacial heat transfer coefficient in reticulate porous ceramics, Int. J. Heat Fluid Flow 29 (2008) 315–326.

[21] E. Maire, P. Colombo, J. Adrien, L. Babout, L. Biasetto, Characterization of the morphology of cellular ceramics by 3D image processing of X-ray tomography, J. Eur. Ceram. Soc. 27 (2007) 1973–1981.

[22] E. Maire, P.J. Withers, Quantitative X-ray tomography, Int. Mater. Rev. 59 (2014) 1–43.

[23] K. Yamamoto, M. Nakamura, H. Yane, H. Yamashita, Simulation on catalytic reaction in diesel particulate filter, Catal. Today 153 (2010) 118–124.

[24] V. Novák, P. Kočí, T. Gregor, J.-S. Choi, F. Štěpánek, M. Marek, Effect of cavities and cracks on diffusivity in coated catalyst layer, Catal. Today 216 (2013) 142–149.

[25] M. Dudák, V. Novák, P. Kočí, M. Marek, P. Blanco-García, G. Jones, Prediction of diffusivity and conversion of n-decane and CO in coated Pt/γ-Al_2O_3 catalyst depending on porous layer morphology, Appl. Catal. B: Environ. 150-151 (2014) 446–458.

[26] H. Giesche, Mercury porosimetry: a general (practical) overview, Part. Part. Syst. Charact. 23 (2006) 9–19.

[27] C.A. Schneider, W.S. Rasband, K.W. Eliceiri, NIH image to ImageJ: 25 years of image analysis, Nat. Methods 9 (2012) 671–675.

[28] J. Schindelin, I. Arganda-Carreras, E. Frise, V. Kaynig, M. Longair, T. Pietzsch, S. Preibisch, C. Rueden, S. Saalfeld, B. Schmid, J.-Y. Tinevez, D.J. White, V. Hartenstein, K. Eliceiri, P. Tomancak, A. Cardona, Fiji: an open-source platform for biological-image analysis, Nat. Methods 9 (2012) 676–682.

[29] H. Darcy, Les fontaines publiques de la ville de Dijon, Dalmont, Paris, 1856.

[30] OpenCFD, OpenFOAM: The Open Source CFD Toolbox, User Guide, OpenCFD Ltd., UK, 2016.

[31] J.O. Van Doormaal, G.D. Raithby, Enhancements of the SIMPLE method for predicting incompressible fluid flows, Numer. Heat Transfer 7 (1984) 147–163.

[32] J.H. Ferziger, M. Peric, Computational Methods for Fluid Dynamics, 3rd ed., Springer-Verlag, Berlin, Germany, 2002.

[33] F. Moukalled, M. Darwish, L. Mangani, The Finite Volume Method in Computational Fluid Dynamics: An Advanced Introduction with OpenFOAM and Matlab, Springer-Verlag, Berlin, Germany, 2016.

[34] N.R. Amundson, R. Aris, A. Varma, The Mathematical Understanding of Chemical Engineering Systems, Elsevier Science, 2014.

[35] S.E. Voltz, C.R. Morgan, D. Liederman, S.M. Jacob, Kinetic study of carbon monoxide and propylene oxidation on platinum catalysts, Ind. Eng. Chem. Prod. Res. Dev. 12 (1973) 294–301.

[36] B.E. Poling, J.M. Prausnitz, J.P. O'connell, et al., The Properties of Gases and Liquids, McGraw-hill, New York, 2001.

[37] N. Wakao, J.M. Smith, Diffusion in catalyst pellets, Chem. Eng. Sci. 17.11 (1962) 825–834.

[38] M. Kaviany, Principles of Heat Transfer in Porous Media, SpringerVerlag, New York, 1995.

[39] J. Happel, H. Brenner, Low Reynolds Number Hydrodynamics: With Special Applications to Particulate Media, Martinus Nijhoff Publishers, Hague, 1983.

[40] T. Bollerhoff, I. Markomanolakis, G. Koltsakis, Filtration and regeneration modeling for particulate filters with inhomogeneous wall structure, Catal. Today 188 (2012) 24–31.